Master's Thesis

STUDY OF THE MANIPULATION AND MECHANICS OF GRAPHENE

Sangjun Oh

Department of Chemistry

Graduate School of UNIST

2019

STUDY OF THE MANIPULATION AND MECHANICS OF GRAPHENE

Sangjun Oh

Department of Chemistry
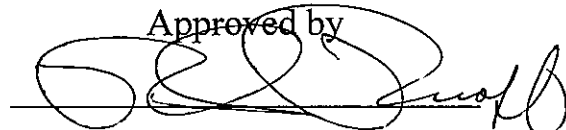
Graduate School of UNIST

Study of the manipulation and mechanics of graphene

A thesis/dissertation
submitted to the Graduate School of UNIST
in partial fulfillment of the
requirements for the degree of
Master of Science

Sangjun Oh

06. 12. 2019 of submission

Approved by

Advisor

Rodney S. Ruoff

UNIST

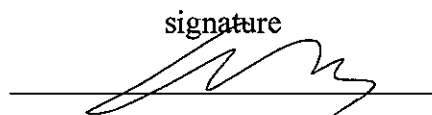# Study of the manipulation and mechanics of graphene

Sangjun Oh

This certifies that the thesis/dissertation of Sangjun Oh is approved.
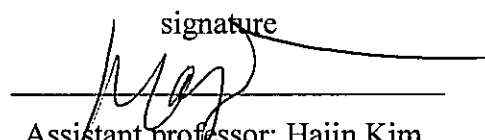
06. 12. 2019

signature

Advisor: Rodney S. Ruoff

signature

Professor: Hyeonsuk Shin

signature

Assistant professor: Hajin Kim

Abstract

Graphene has been the focus of significant research attention for a decade due to its remarkable mechanical, electrical, and optical properties. It has also been reported that modifying the morphology of a graphene sheet by introducing curves or wrinkles can tune these properties. In Chapter I, we present a technique which can remotely control graphene's morphology using a magnetic tweezer. Graphene was anchored to a chromium post and a magnetic iron patch was deposited on the graphene edge. In this way, we modified the morphology of graphene by application of an external magnetic field. We also demonstrated a microfluidic device which could be switched on and off by magnetic manipulation of graphene.

Although graphene's mechanical properties show very high values, the measured response in the macroscale is much lower than theoretical and experimental microscale values. When the length scale increases, the probability of encountering defects becomes higher, resulting in lower performance (if there are defects—and evidently there are). In Chapter II, we have attempted to determine the nature of graphene's mechanical performance by identifying regions that contain defects so as to determine their exact effect on the mechanical performance using the microelectromechanical system "Push-to-Pull stage" inside a scanning electron microscope.

Contents

List of Figures

Chapter 1

Chapter 2

List of Schemes

Chapter 1.

Chapter 2.

List of Abbreviations

DMSO	Dimethylsulfoxide
SDBS	Sodium dodecylbenzenesulfonate
PMMA	Polymethymethacrylate
PDMS	Polydimethylsiloxane
IPA	Isopropyl alcohol
MEMS	Microelectromechanical system
PtoP	Push-to-Pull
FIB	Focused ion beam
DIC	Digital Image Correlation

Chapter 1. Graphene manipulation using a magnetic tweezer

1. Introduction

Two-dimensional (2D) nanomaterials such as graphene, hexagonal boron nitride, and molybdenum disulfide, have been studied due to their promising applications in transistors [1], supercapacitors [2], and photodetectors [3]. In the majority of these studies, the devices were fabricated based on a planar geometry. However, in emerging applications such as wearable electronics, stretchable biological sensors could benefit from curved and folded architectures [4, 5]. Additionally, it is also reported that a significant change in the physical and chemical properties could be caused by introducing curvature, wrinkles, or folded structures in graphene. [6, 7].

There have been a number of previous reports of folding or wrinkling graphene due to the very low bending stiffness of graphene. [8] For example, previous studies have made curves or folds in the graphene through the action of interfacial forces. [9] In other works, graphene has been folded and crumpled in water by mechanical stimulation using ultrasonication [10] or folding was induced by ablation with a femtosecond laser [11]. In these studies, the morphology was manipulated without precision or reproducibility and they required harsh conditions (ultrasonication or high energy laser pulses).

Theoretical studies have suggested that if folding could be precisely controlled, 3-dimensional geometries such as capsules, flowers, rings, or boxes could be produced. [12, 13] One reported experimental approach has been to coat graphene onto a thermoresponsive polymer so that its morphology could be controlled reversibly by changing the temperature. [14] Although this method resulted in shape control, graphene is required to be attached to a substrate and manipulation is limited by stretching or contraction of the substrate.

Manual folding of kirigami-patterned graphene has been demonstrated, and various shapes such as springs, stretchable electrodes, and hinges have been studied using external mechanical forces. Additionally, the graphene could also be twisted by application of an external magnetic field. [15] Graphene can be "manipulated" with a magnetic field independent of a substrate and controlled and remote manipulation can be targeted. Here, we report our own strategy to manipulate the morphology of graphene by using a magnetic tweezer system and demonstrate a potential application in microfluidics.

2. Experimental Method & Materials

2.1. Materials

Microscope coverslips were purchased from Electron Microscopy Sciences (EMS). All metal sources, including copper (99.997%), chromium (99.99%), and iron (99.99%) were purchased from iTasco. Polymethylmethacrylate (PMMA), AZ 5214E, LOR 5A, and SU-8 2015 photoresists, as well as AZ 300MIF developer were purchased from Microchem. Sodium hydroxide (97%), dimethyl sulfoxide (DMSO) (99.9%), ammonium persulfate (98%), sodium dodecylbenzenesulfonate (SDBS) (technical grade), and trichloro(1H,1H,2H,2H-perfluorooctyl)silane (97%) were purchased from Sigma-Aldrich. For synthesizing polydimethylsiloxane (PDMS) sheet, SYLGARD 184 A (elastomer base) and B (curing agent) were purchased from Dow Corning.

2.2. Substrate preparation

First, the coverslip was cleaned by immersing in acetone, isopropyl alcohol (IPA), and sodium hydroxide (1 M) sequentially for 20 minutes each with sonication. Then, a copper layer was deposited on the coverslip (40 nm) by E-beam evaporation (Temescal). After deposition, the photolithography process was done in the cleanroom. The photoresist, AZ5214E, was spin-coated on the substrate at 4000 rpm for 30 seconds and the sample was heated for 3 minutes and 10 seconds at 105 °C. After, 90 mJ of UV-light was irradiated on the sample by a MIDAS photo aligner (MDA 400) and the sample was then submerged in the developer (AZ 300MIF). It was agitated for 1 minute to develop the pattern, then immersed in ammonium persulfate solution (0.3M) to etch the unnecessary copper. Next, the chromium layer for anchoring one side of the graphene ribbon was deposited on the substrate and the photoresist was then removed by immersing the sample in DMSO solvent at 60°C for realizing the pattern. The sample was finally washed first with IPA and then deionized water (DI water). The result of this process is described in **Figure 1**.
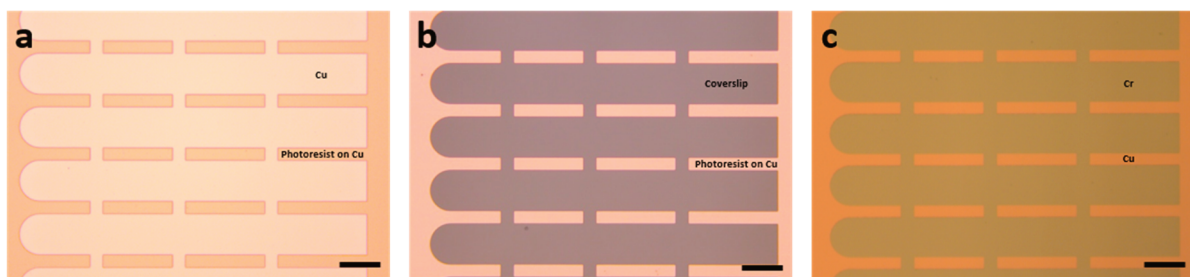
Figure 1. Optical image of the sample at different stages of photolithography (a) after the patterning of photoresist on the Cu coated coverslip. (b) After the etching of unwanted Cu layer. (c) After the Cr deposition and removing the photoresist. All scale bars are 50 μm.

2.3. Graphene transfer and fabrication of graphene micro ribbon

Graphene was grown by chemical vapor deposition on both sides of a home-made single crystalline copper foil. [16] [17] The graphene coated copper foil was cut into 1x1 cm pieces and PMMA was spin-coated on one side of the graphene/copper foil. Next, the foil was floated on ammonium persulfate (0.3M) solution for 10 minutes with the PMMA coated side being the top surface. Next, the assembly was then picked up to remove the graphene on the non-PMMA coated side by scrubbing the surface. The foil was then floated on the etchant again to remove all of the copper, then the graphene-PMMA composite was washed of etchant residues by transferring and floating on a separate container of DI water (30 minutes), repeating twice. The composite was transferred on top of the photolithographically prepared substrate and dried overnight in ambient conditions. To ensure conformal contact with the substrate, it was heated at 90 ˚C on the hot plate and cooled down. The sample was soaked for 30 minutes in acetone to remove the PMMA and the transferred graphene assembly underwent photolithography in the same way as described in **section 2.1** but using a different mask to pattern the graphene micro ribbon. The sample was then treated by hydrogen plasma for 1 minute to remove the unnecessary regions of graphene from the device, and the photoresist that covered the graphene was removed by brief immersion in acetone with sonification (3 seconds). Finally, the sample was rinsed by IPA and DI water, sequentially. The optical images of this process are shown in **Figure 2**.
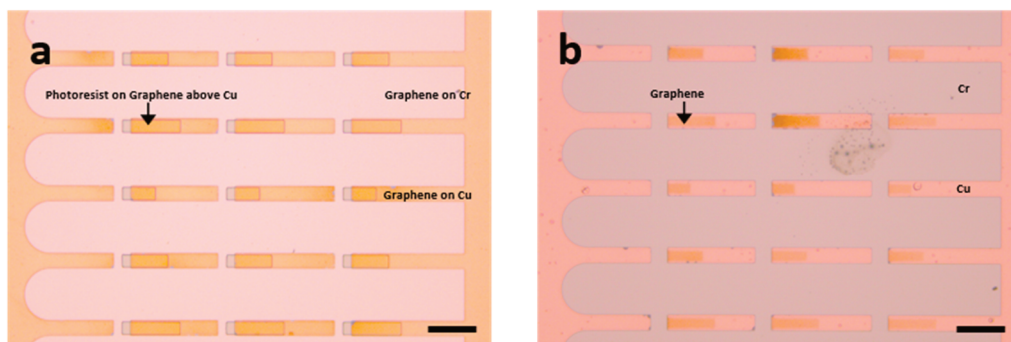
Figure 2. Optical images of the patterning of graphene micro ribbons; (a) patterned photoresist on the graphene layer (note graphene exists in the entire region) (b) patterned graphene micro ribbon after removing the photoresist. Scale bars are 25 μm.

2.4. Attachment of iron pad

To attach the iron pad to the graphene micro ribbon, photoresist (LOR-5A) was spin-coated (4000 rpm for 30 seconds) on the substrate which was prepared in **section 2.3** and heated at 170 °C for 6 minutes. Next, a second photoresist (AZ5214E) was spin-coated on the substrate at 4000 rpm for 30 seconds and the sample was then heated for 3 minutes and 10 seconds at 105 °C. After that, 90 mJ of UV-light was irradiated on the sample and then immersed in the developer (AZ 300MIF) and agitated for 1 minute to develop the pattern. Using e-beam evaporation, 5 nm of Cr was deposited as an adhesion layer, followed by 60 nm of Fe for the magnetic spot, then a final 5 nm Cr to protect the Fe layer from the copper etchant. Finally, it was immersed in DMSO at 60 °C to remove all remaining photoresist and the iron patch pattern was successfully deposited on the edges of each graphene ribbon.
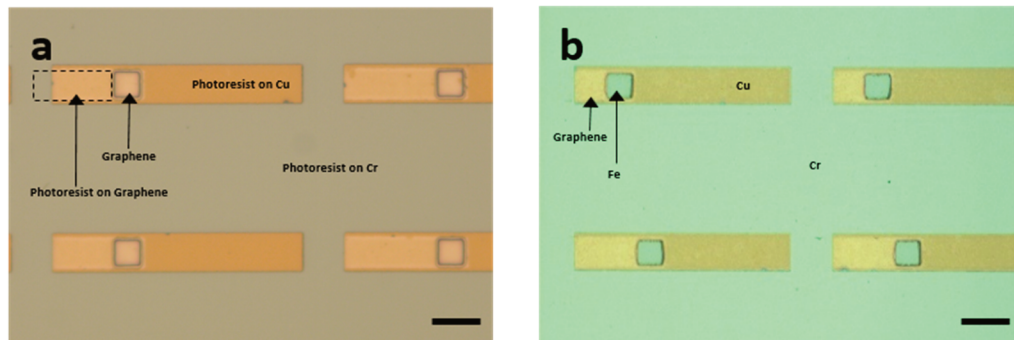
Figure 3. Patterning for magnetic spot deposition. (a) Patterned photoresist (b) Fabricated graphene micro ribbon with iron patch. All scale bars are 25 μm.

2.5. Fabrication of microchannel in SU-8 photoresist

To make the reservoir and channel for microfluidics studies, SU-8 2015 was spin-coated on the prepared device at 3000 rpm for 30 seconds to make a thickness of 15 μm. The sample was baked at 95 ˚C for 3 minutes and 140 mJ of UV-light was irradiated on the sample. After that, the sample was again baked at 95 ˚C for 4 minutes then submerged in SU-8 developer for 1 minute and 30 seconds. The result of this process is described in **Figure 4**.
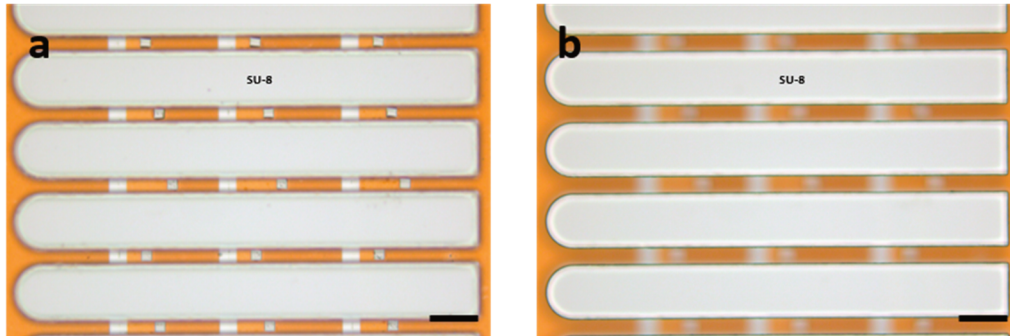
Figure 4. Fabricated microchannel in SU-8 photoresist. The height of the SU-8 sidewall could be recognized by the difference of the focus between (a) and (b). All scale bars are 25 μm.

2.6 Characterization

Inspection of photoresist patterns was done after each step with optical microscopy (ZEISS Axio Imager 2). The provided graphene sample and the micro ribbon graphene were characterized by WITec Raman spectroscopy (Alpha300M) and its morphology was investigated by FEI scanning electron microscope (SEM) (Verios 460). The thickness of each metal layer made with the E-beam evaporator was measured by atomic force microscopy (AFM) (Bruker DIMENSION icon with ScanAsyst).

2.7 Synthesis of PDMS sheet

To synthesize the PDMS sheet, first the elastomer base and curing agent were mixed thoroughly in a 10:1 ratio and kept in the desiccator to remove the bubbles. Next, trichloro(1H,1H,2H,2H-perfluorooctyl)silane was vapor-deposited in a vacuum chamber for 30 minutes to create a non-stick surface on a silicon wafer which allowed easy detachment of cured PDMS. After all the bubbles were removed from the PDMS solution, it was poured on the wafer and spin-coated at 400 rpm for 60 seconds. Then the PDMS coated Si wafer was cured in an oven at 90˚C for 1 hour and the PDMS sheet removed by peeling.

2.8 Releasing of Cu layer and graphene manipulation
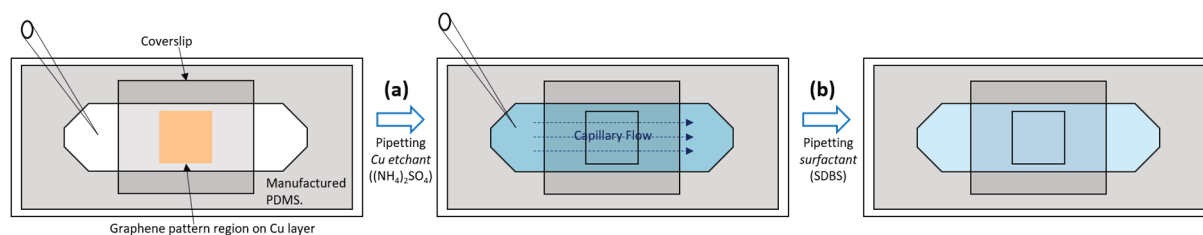
Scheme 1. (a) Etching of Cu layer by injection of ammonium persulfate. (b) Exchange the solvent from etchant to surfactant (SDBS).

Due to water surface tension creating liquid drops of substantial height that interfered with operation of the permanent magnet in magnetic tweezer system and to induce capillary flow to enhance liquid exchange, we encased sample under a coverslip with a small gap of ~170 μm. This distance was defined by the thickness of a PDMS sheet used as a spacer and was prepared as described in **section 2.7**. In the case of the graphene ribbon patterns as described in **Figure 6a-e**, regions of PDMS where the micro ribbon would normally lie were removed by blade (see **Scheme 1a**). A coverslip was then placed on the PDMS to create a channel for liquid flow. In the case of the device which containing micro channel (design of **Figure 6f**), a flat PDMS sheet covered the microchannel region of the device in the place of a coverslip. Before manipulation, to make the graphene "free standing", the copper sacrificial layer was released by injection of a solution containing 0.3 M ammonium persulfate diluted and 3mM of SDBS. The SDBS acts to reduce the adhesion between graphene and the coverslip's surface and to prevent the graphene from permanently sticking with itself. [15] The etchant was flowed across the device and removed by absorbing into a Kimtech tissue. The solution was gradually changed into a pure SDBS solution by repeating the injection and draining process.

The home-built magnetic tweezer system (made by Dr. Kipom Kim in Korean Brain Research Institute) was made to interact with the sample by both varying the height and rotating of the permanent magnet pair above the sample. All of these processes were observed by digital camera and the bright field images were taken under LED illumination. The configuration of the magnetic tweezer is depicted in the **Figure 5**.
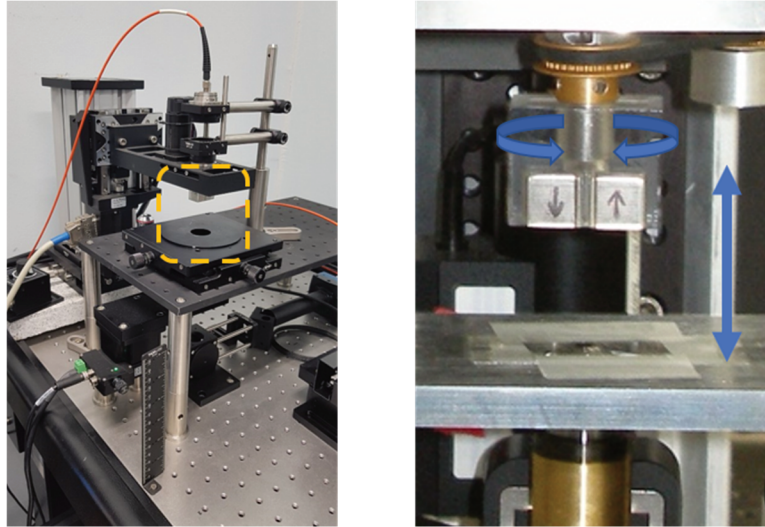
Figure 5. (a) The home built magnetic tweezer set-up. The sample is loaded on the stage and observed by digital imaging. Bright field images are illuminated by an LED. (b) The region highlighted by orange rectangle in (a) showing permanent magnet fixed in the holder and the movement of the tweezer which can be controlled by both rotation and up and down movement.

3. Result & Discussions

3.1 Optical images of graphene array and the Raman spectra, SEM, and AFM

According to the photomask's pattern, various types of graphene pattern could be realized. By designing different types of features in the photomasks, we modified the shape and length scale of the graphene patterns. Various configurations we have attempted are shown in **Figure 6**.
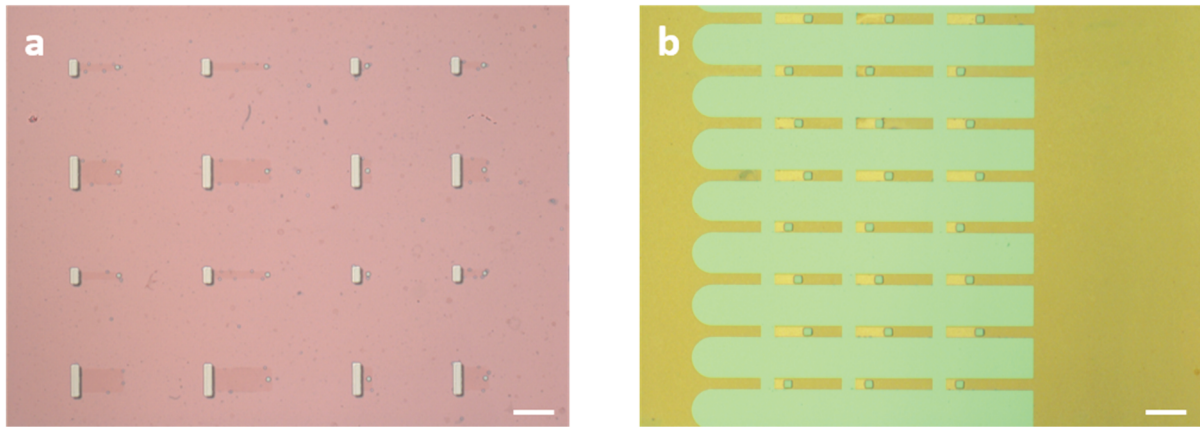
Figure 6. Optical microscope image of realized various size of graphene pattern. (a) Micro ribbon type graphene ribbons showing different size and aspect ratio. (b) Graphene micro ribbon pattern for microfluidics testing. All the scale bars are 50 μm.

After device fabrication, we used a combination of SEM, AFM, and Raman spectroscopy to inspect device fabrication and to find the location of graphene. Images in **Figure 7** correspond to the device as shown in **Figure 6f**.
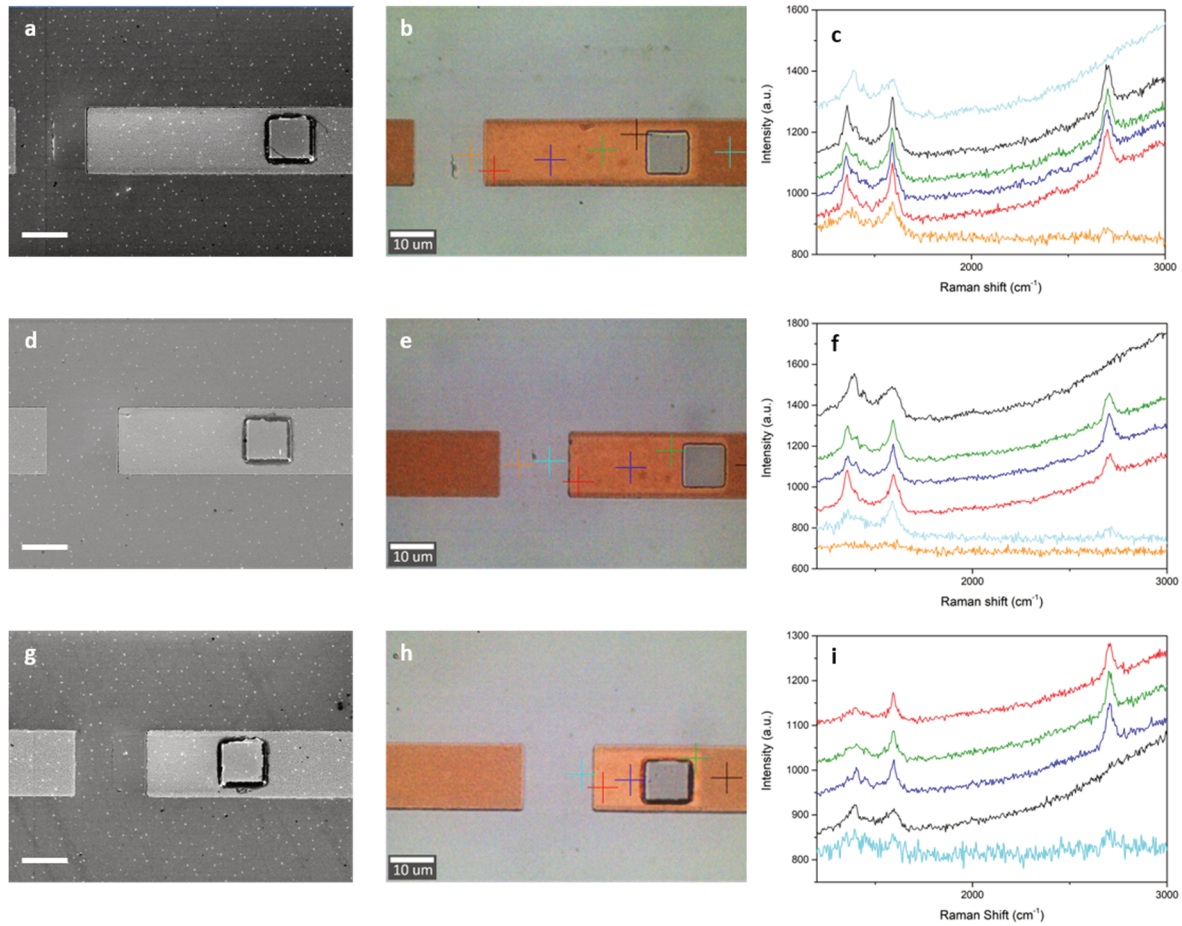
Figure 7. (a-c) SEM image, optical microscope image, and corresponding Raman spectra of 1:4 aspect ratio of graphene micro ribbon with iron patch. (d-f) 1:3 aspect ratio (g-i) 1:2 aspect ratio. All scale bars are 10 μm.
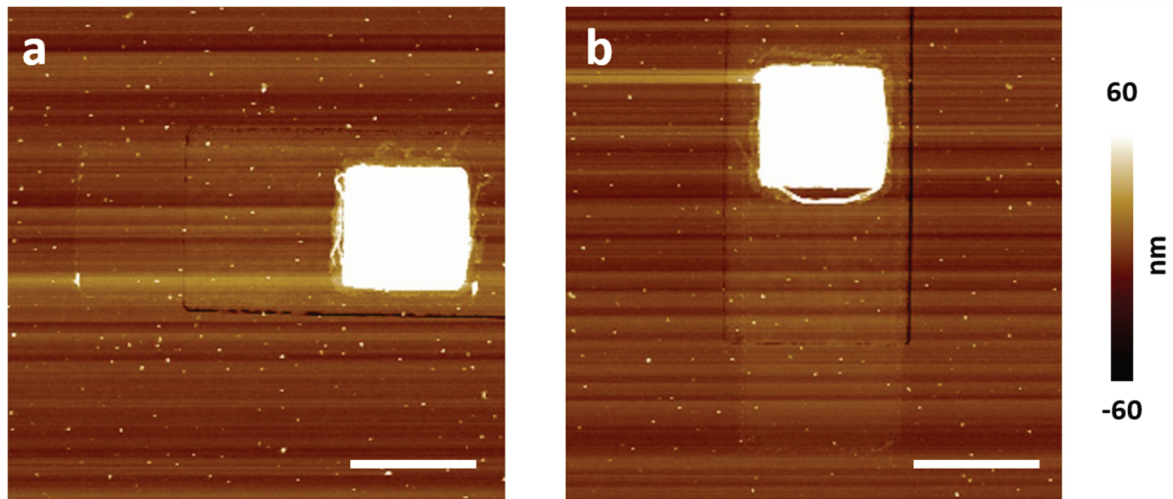
Figure 8. AFM topography images of 1:2 aspect ratio graphene micro ribbon scanned in (a) parallel and (b) perpendicular direction to the ribbon's length. **Figure 8b** was taken to show the graphene's edge clearly on copper layer. All scale bars are 10 μm.

3.2 Magnetization of iron patch and Neodymium magnet in magnetic tweezer

Before operation of the magnetic tweezer, we measured the magnetic force exerted by the permanent neodymium magnet (N35 grade) attached to the tweezer by a HIRST gaussmeter (GM08). According to the configuration of the fixed magnets in the holder, the magnetic force was measured at the gap region between two magnets. The force profile according to the distance is described in the **Figure 9a** and this data closely matched the simulated data by software, FEMM 4.2 as shown in the **Figure 9b**.
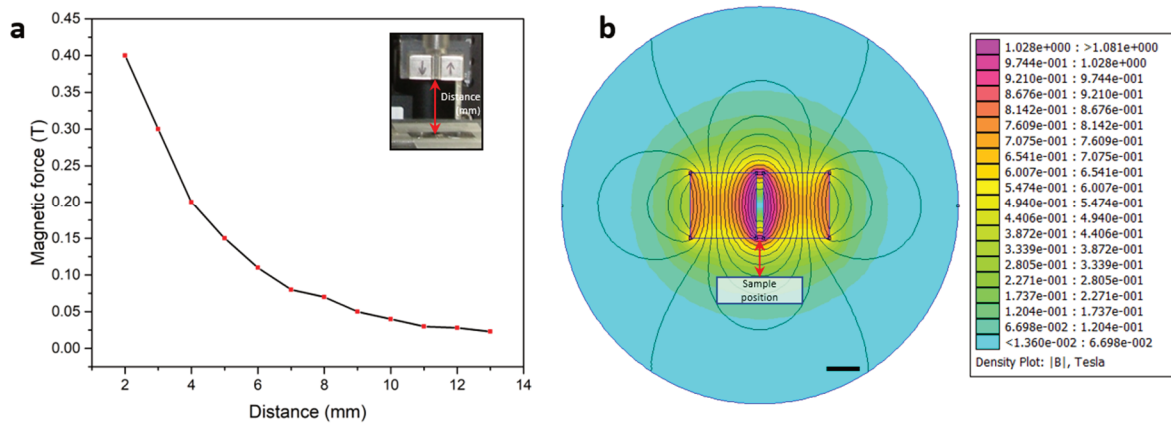
Figure 9. (a) Magnetic tweezer's magnetic force as a function of the distance from the sample. (b) Cross-sectional contour map of magnetic field intensity around the magnetic tweezer's a pair of permanent magnets simulated by FEMM 4.2 software. The scale bar is 5 mm.

3.3 Images of graphene's behavior according to the rotation of magnetic field.

In this section, I describe the graphene behavior in response to the magnetic tweezer's rotating magnetic field and present snapshots of the recorded video. The full video is available as supplementary information downloadable from the following link in ScholarWorks@UNIST. [https://scholarworks.unist.ac.kr/handle/201301/26844]

3.3.1 Micro ribbon graphene with one iron dot
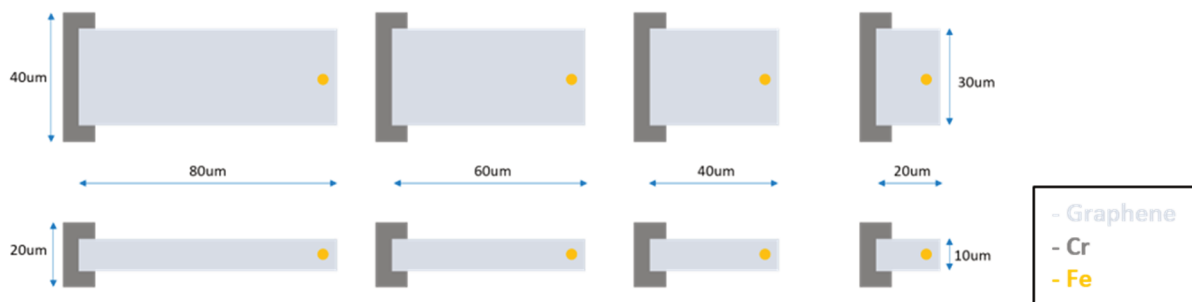
Scheme 2. Micro ribbon graphene with one iron dot.

This device is a basic design to examine the effect of an external magnetic force in controlling graphene's morphology. The geometry of the graphene pattern with iron dots (magnetic spots) is described in the **Scheme 2** and snapshots of the graphene micro ribbon reacting to the rotation of magnetic field are shown in **Figure 10**. (**Video S1**)
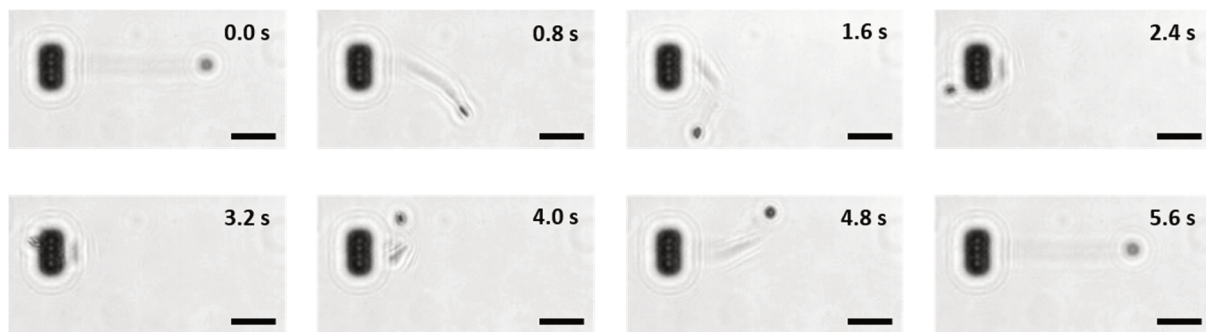
Figure 10. Snapshots of the graphene micro ribbon according to the rotation of magnetic field. All scale bars are 20 μm.

As shown in these snapshots, as the attached iron dot is responding to the external magnetic field, the graphene ribbon and the iron rotates. Although the iron dots are rotating consistently, the graphene ribbon is not twisted but instead shows a 'slip and stick' motion. In this experiment, we have demonstrated that graphene manipulation using external magnetic field is feasible.

3.3.2 Larger micro ribbon graphene with an iron patch

Scheme 3. Enlarged graphene micro ribbon with an iron patch.

This type of graphene ribbon is similar to the basic design of micro ribbon pattern in **section 3.3.1**. The iron dot in this section is however replaced by a large iron "patch" to increase its interaction with the magnetic field and the graphene ribbon's size is also increased. The geometry is described in the **Scheme 3** and the snapshots of the pattern according to the rotation of external magnetic field are described in the **Figure 11**. (**Video S2**)
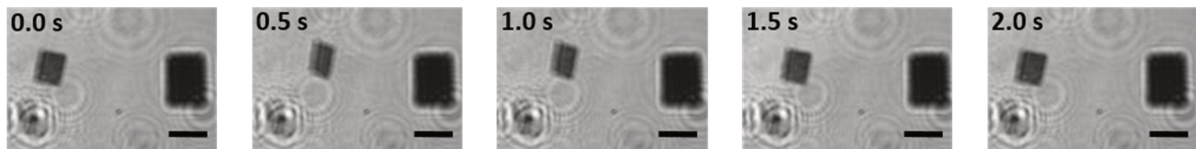
Figure 11. Snapshots of the movement of enlarged graphene micro ribbon. All scale bars are 30 μm.

In the motion snapshots, the ribbons repetitively move to the right and left sides, following the rotation of magnetic field. Because of their increased width compared to the previous example, the rotation does not happen, but instead there is this lateral movement in the horizontal plane.
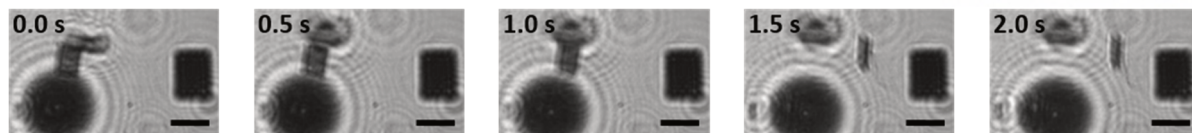
Figure 12. Snapshots of the elevation of the graphene ribbon when the permanent magnet is brought closer to the sample. All scale bars are 30 μm.

We also observed that the graphene ribbon can be "raised up" by bringing the permanent magnet closer to the graphene ribbon in the aqueous SDBS solution, see **Figure 12**. (**Video S3**) When the external field was not applied, the graphene ribbon resided on the coverslip surface. When the external magnetic field was applied the iron patch was raised up, bending the graphene micro ribbon. Based on this behavior, we thought that the graphene ribbon could act as a switch to open and close a microfluidic channel by rotating it per 90° so that it can turn on and off the liquid flow.

3.3.3 Micro ribbon graphene with one iron patch for microfluidics testing

Before we tested the graphene switch, a microfluidic channel of 25 μm thickness was tested by flowing 3 μm size colloidal particles dispersed in 3mM SDBS solution as a control experiment. The images in **Figure 13** are snapshots from this flow. (**Video S4**)
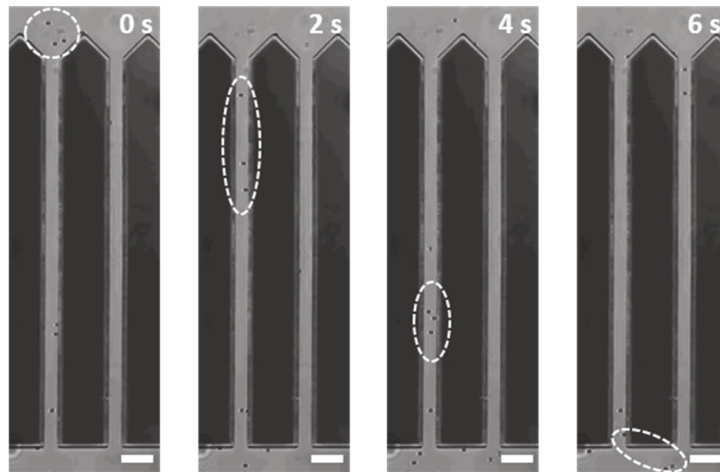
Figure 13. Snapshots of the flow of SDBS shown by colloidal particles movement in the microchannel. All scale bars are 30 μm.

We can observe colloidal particles moving through the microfluidics channel, indicating this microchannel model is suitable to use with the graphene switch. We fabricated a device incorporating the graphene switch in the microfluidic channel and this is presented schematically in **Scheme 4**. When the magnetic field is applied to the graphene ribbon, the graphene will be lifted as described in the **section 3.3.2**, inhibiting flow in the channel. (**Scheme 4a**) However, if the field's direction is rotated in 90°, the iron pad will also rotate causing the graphene to twist and allow flow through the channel to occur (**Scheme 4b**). The operation of the graphene switch is described in **Figure 14**. (**Video S5**)
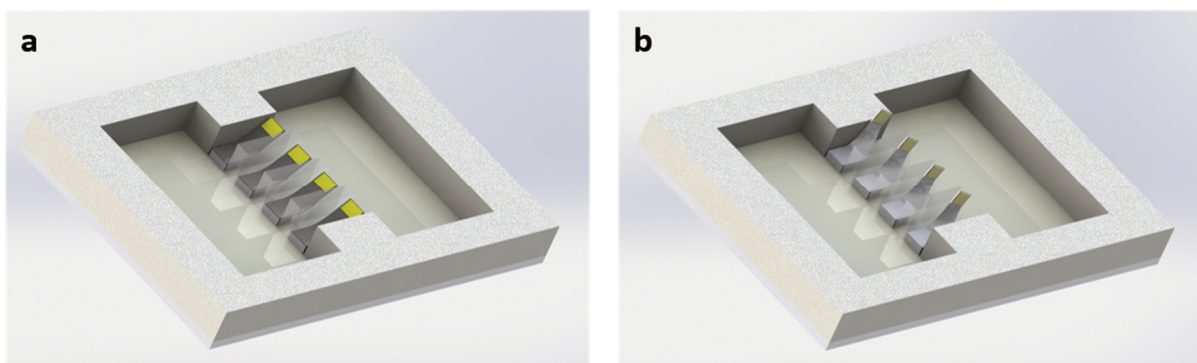
Scheme 4. (a) Raised graphene ribbon's state without an external magnetic field will block the channel. (b) Twisting the graphene ribbon by external magnetic field opens the channel to flow.
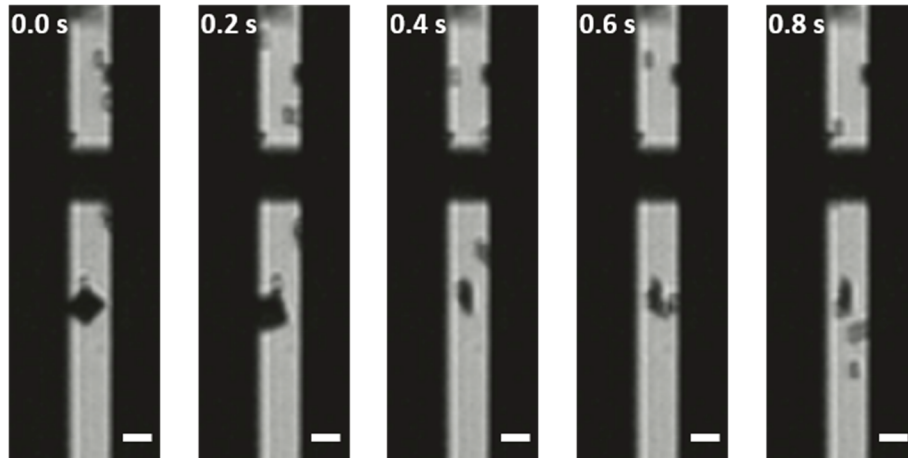
Figure 14. Snapshots of graphene micro ribbon switch operation. When the direction of magnetic field was changed in 90˚, the colloidal particles flew faster than before opening the gate. All scale bars are 10 μm.

According to the motion snapshots, at the original state, the micro channel was roughly blocked by the elevated graphene ribbon and iron patch, inducing the slow flow of the colloidal particles. When the magnetic field was rotated in 90˚, we could observe the colloidal particles flow through the micro channel faster than before by twisting the graphene ribbon and opening the gate, which showed our graphene switch's potential in the microfluidics. A microfluidic switch of this type can be remotely operated without any mechanical deformation of the channel's exterior shape.

3.4 Conclusion and suggestions for further research

In this chapter, the manipulation of various types of graphene micro-ribbon by rotation of magnetic field has been presented, and a microfluidic device with a graphene switch that could potentially control the fluidic flow was made and tested. Due to the current configuration of the magnetic tweezer, the magnet's movement was limited to rotation and back-and-forth motion normal to the device plane. This motivated our building a new configuration of magnetic tweezer and it is under construction and shown in **Figure 15**.
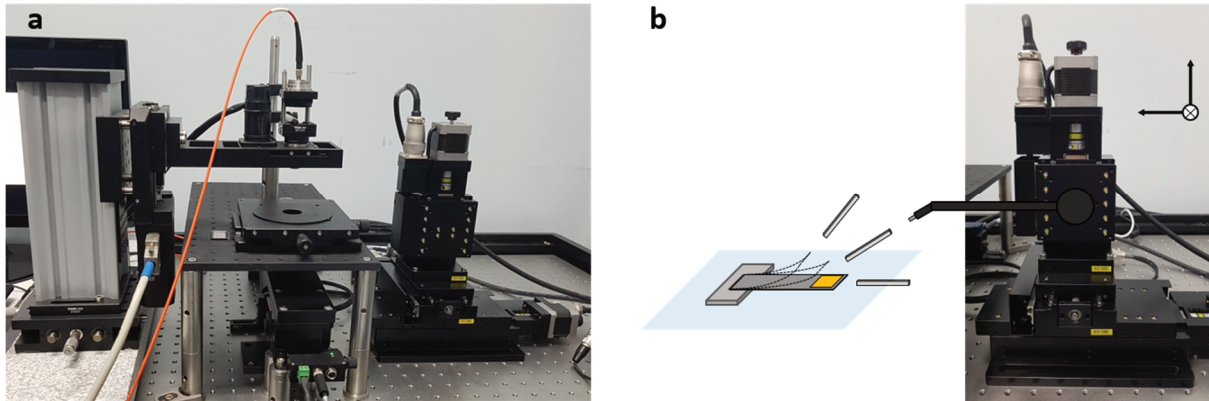
Figure 15. (a) The image of newly constructed magnetic tweezer. (b) The planned new configuration of magnetic tweezer. Additional x-, y- and z- axis actuators are installed beside the original magnetic tweezer system for more precise manipulation.

In the updated system, x-, y- and z- axis actuators are newly added inside the magnetic tweezer system. This configuration will allow the permanent magnet to approach along the device plane. With the new actuator, a magnetized particle can be more precisely moved in any direction. In the new system, the permanent magnet can more closely approach the graphene ribbon and its magnetic field can more readily magnetize the particle for better manipulation.
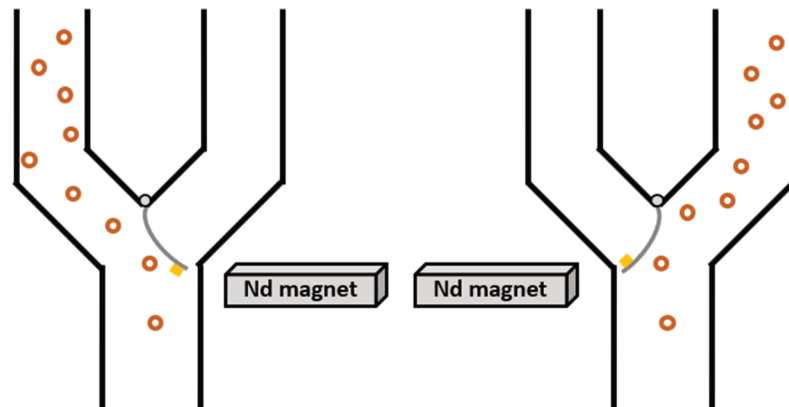
Figure 16. Two different pathways for the operation of a micro scale sorting machine.
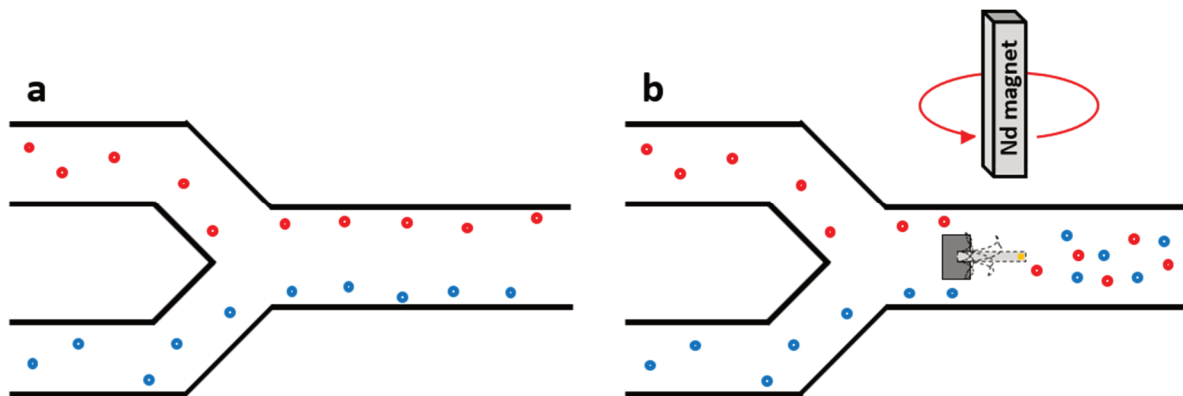
Figure 17. Micro scale mixer. (a) Flow of 2 different particles before the installation of the micro mixer and (b) expected flow using the mixer.

We could also foresee other microfluidic components. One such component is a micro-scale sorting machine (**Figure 16**). If the microfluidic channel contains a forked pathway, then we can direct flow along a particular path by positioning the graphene ribbon so that it can block either path.

In microfluidic channels, when particles from two different pathways merge into one channel, they rarely mix well but instead flow along the channel walls until they are perhaps finally mixed by diffusion. We propose another microfluidic component that will allow nearly instantaneous mixing. If we use magnetic tweezer rotation to induce a spinning motion of graphene, this could allow rapid mixing in the microfluidic channel (**Figure 17**). These proof-of-concept tests have potential to be applied in microfluidic devices that are being explored in drug delivery and pharmaceutical fields.

4. References

1.   Schwierz, F., *Graphene transistors.* Nat Nanotechnol, 2010. **5**(7): p. 487-96.

2.   Singh, V., et al., *Graphene based materials: Past, present and future.* Progress in Materials Science, 2011. **56**(8): p. 1178-1271.

3.   Gupta, A., T. Sakthivel, and S. Seal, *Recent development in 2D materials beyond graphene.* Progress in Materials Science, 2015. **73**: p. 44-126.

4.   Rogers, J.A., T. Someya, and Y. Huang, *Materials and mechanics for stretchable electronics.* Science, 2010. **327**(5973): p. 1603-7.

5.   Kabiri Ameri, S., et al., *Graphene Electronic Tattoo Sensors.* ACS Nano, 2017. **11**(8): p. 7634-7641.

6.   Deng, S.K. and V. Berry, *Wrinkled, rippled and crumpled graphene: an overview of formation mechanism, electronic properties, and applications.* Materials Today, 2016. **19**(4): p. 197-212.

7.   Zhu, W., et al., *Structure and electronic transport in graphene wrinkles.* Nano Lett, 2012. **12**(7): p. 3431-6.

8.   Wei, Y., et al., *Bending rigidity and Gaussian bending stiffness of single-layered graphene.* Nano Lett, 2013. **13**(1): p. 26-30.

9.   Wang, B., et al., *Controlled Folding of Single Crystal Graphene.* Nano Lett, 2017. **17**(3): p. 1467-1473.

10.   Zhang, J., et al., *Free folding of suspended graphene sheets by random mechanical stimulation.* Phys Rev Lett, 2010. **104**(16): p. 166805.

11.   Silvestre, I., et al., *Folded graphene nanochannels via pulsed patterning of graphene.* Applied Physics Letters, 2015. **106**(15).

12.   Patra, N., B. Wang, and P. Kral, *Nanodroplet activated and guided folding of graphene nanostructures.* Nano Lett, 2009. **9**(11): p. 3766-71.

13.   Zhu, S. and T. Li, *Hydrogenation-assisted graphene origami and its application in programmable molecular mass uptake, storage, and release.* ACS Nano, 2014. **8**(3): p. 2864-72.

14.   Xu, W., et al., *Ultrathin thermoresponsive self-folding 3D graphene.* Sci Adv, 2017. **3**(10): p. e1701084.

15.   Blees, M.K., et al., *Graphene kirigami.* Nature, 2015. **524**(7564): p. 204-7.

16.   Jin, S., et al., *Colossal grain growth yields single-crystal metal foils by contact-free annealing.* Science, 2018. **362**(6418): p. 1021-1025.

17.   Wang, B., et al., *Camphor-Enabled Transfer and Mechanical Testing of Centimeter-Scale Ultrathin Films.* 2018. **30**(28): p. 1800888.

18.   West, A.R., *Solid state chemistry and its applications.* Second ed. 2014, Chichester: John

Wiley & Sons, Ltd.

Chapter 2. Mechanical test of graphene-fold using MEMS stage

1. Introduction

1.1 Introduction

Single layer graphene has been reported to have very high mechanical performance but at only micron length scale, as obtained by different experimental approaches. The authors of a study of the mechanical response to nanoindentation of micron-scale membranes reported the Young's modulus (1.0 TPa) and fracture strength (130 GPa) values. [1] At the micron length scale, there is a high probability that the tested region could be defect-free resulting in very high strength values. When measurements are performed at the macroscale (e.g., centimeter scale) such as recently done by the Ruoff group using a new method, both the average values of the room temperature modulus (793 GPa) and fracture strength (3.4 GPa) of single crystalline graphene were lower than reported micro-scale values. [2] Evidently at centimeter scale for chemical-vapor-deposition (CVD) grown graphene tested to date, there are flaws (defects—holes essentially) that reduce the strength from the "ideal value". While some may suggest that it is the grain boundaries in polycrystalline graphene that extremely limit its strength, this can be the possible case as the introduction of, e.g, Thrower-Stone-Wales type defects (pentagon-heptagon pairs replacing hexagon-hexagon, due to a bond rotation) can change the strength from 130 GPa to 70 GPa. [3, 4] It is also reported that the polycrystalline graphene's mechanical strength (3.33 GPa) is not much different with the single crystalline one (4.50 GPa). [2]

For the case of chemical vapor deposition (CVD) grown graphene, the discovery of the presence of parallel linear "fold" structures in the graphene was reported recently by the Ruoff group. [5] They appear due to the differing thermal contraction between graphene and the copper foil as the foil that the graphene has been grown on at 1070 °C, is then cooled to room temperature. These fold structures have a width of ~100 nm and are spaced at about 20-30 μm apart. Per studies by other team members in the Ruoff group (Ming Huang, Da Luo, Meihui Wang) fold structures also contain broken regions (cracks). [Manuscript in preparation] Such cracks in the graphene fold structure can lower the overall mechanical properties of the CVD grown single crystal graphene—but it is not known if these are the critical flaws or not. We can estimate this by calculation of stress concentration factor, which will be described in the following section.

1.2 Study of stress concentration factor

When the crack exists in the material, the applied stress is focused at the tip of the crack. In the case of brittle fracture where the crack propagates very rapidly with little plastic deformation, we can apply the linear elastic fracture mechanics (LEFM). Through the Inglis's formula [6], we can calculate how much stress is loaded at the tip of the crack when certain stress is applied to the material in the uniaxial tensile loading. The shape of the crack is usually assumed as a Griffith model which is an ellipse as shown in **Scheme 1**. [7] Following equation (1) is describing the Inglis's formula.

Scheme 1. Griffith model of a crack.

$$\sigma_{Max} = \sigma \left(1 + \frac{2a}{b}\right) \cong \sigma \, \frac{2a}{b} = 2\sigma \sqrt{\frac{a}{\rho}} \qquad (\rho = b^2/a, \; b \ll a) \qquad (1)$$

where σ_{Max} is the loaded stress at the tip of the crack, σ is the applied stress at the material, and 2a and 2b are the major and minor axes of the ellipse, respectively. The σ_{Max}/σ is defined as stress concentration factor. We note that if the a is much larger than b, 2a/b becomes the stress concentration factor. This factor simply describes the geometric effect of the crack on the local stress such as at the tip of the crack.

However, when we handle the crack where the b value is infinitesimal such as atomically thin crack, we account the problem that failure of material must occur at the physically unreasonable zero load. Therefore, to supplement this problem, quantized fracture mechanics (QFM) can be utilized to understand the crack instead of the continuum based LEFM. According to the QFM, the loaded stress at the tip of the crack can be quantized and calculated as equation (2). [8]

$$\sigma_f(n) = \sigma_c \sqrt{1 + \frac{\rho}{2a}} \, (1+n)^{-1/2} \qquad (n > 0) \qquad (2)$$

where $\sigma_f(n)$ is the fracture stress of material which contains an n-atom defect linearly, σ_c is ideal strength, a is fracture quantum which is lattice spacing and close to the atomic size, and ρ is the crack tip radius. Therefore, if we figure out the length of the crack, we can calculate the stress that the material containing the crack can endure.

In the following section, we are going to apply this concept to estimate the effect of the cracks in the fold structures to the overall material.

1.3 Application of stress concentration factor to the crack in the graphene fold structure

The previously mentioned graphene fold structure is obviously shown in our experimental data of dog-bone specimen (#4) fabrication. The SEM image of broken fold structure and its schematic is shown in **Figure 1**.
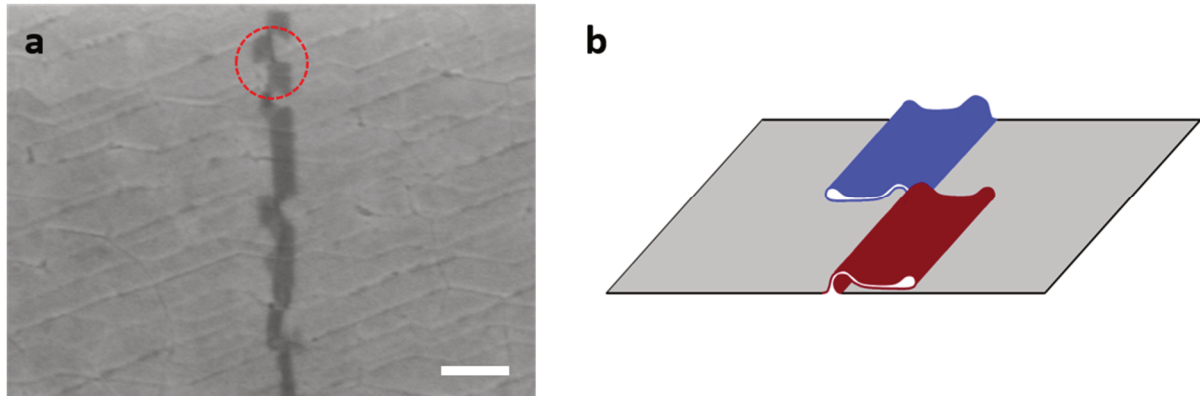
Figure 1. (a) SEM image of broken spot in sample #4. (b) The schematic showing the broken fold. A scale bar is 500 nm.

During the cooling step in graphene growth by CVD, the graphene wrinkle is formed and when it reaches to the certain height (~300 nm), it starts to be laid. The graphene is broken when a part of raised graphene wrinkle lays down into righthand side while another one lays down into the opposite side. Here, the crack happens at the tearing part which is indicated by red dashed circle in **Figure 1a**.
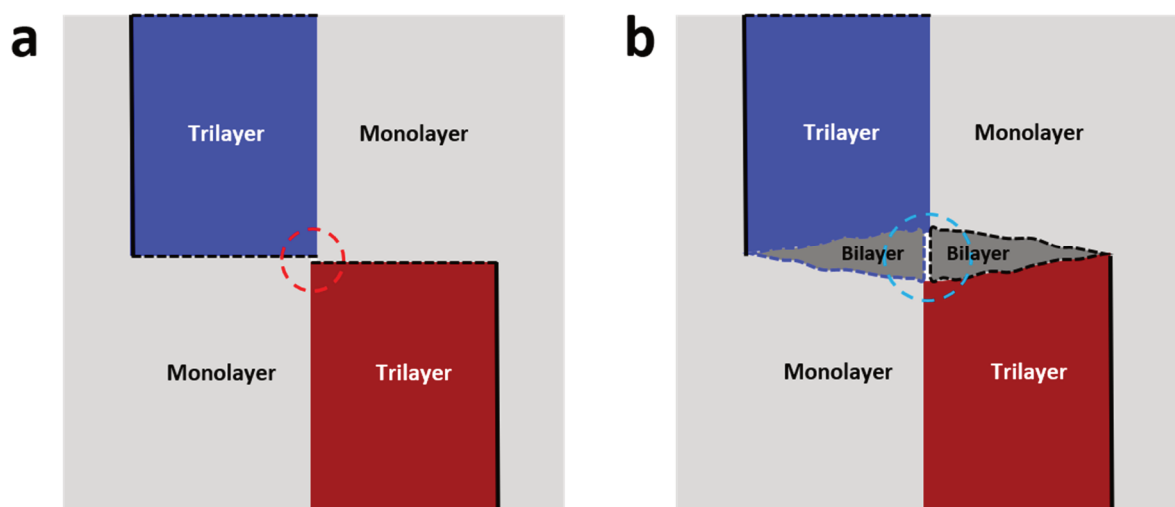
Scheme 2. Differently broken graphene fold structure. (a) Formation of point vacancy defect. (b) Formation of linear crack defect. These schemes are top-view of **Figure 1a**.

During the tearing process, if the wrinkle is broken clearly into two opposite directions, it is expected that there is a point vacancy at the broken spot which is highlighted by the red dashed circle in **Scheme 2a**. It is reported that the point vacancy can lower the endurable maximum stress from σ_c to 0.836 σ_c based on the molecular dynamic simulation in QFM where the σ_c is the intrinsic strength of graphene. [4] From this theoretical calculation, it seems that the point vacancy cannot influence significantly to the overall graphene's mechanical performance. However, it has been reported that when vacancy defects are introduced at a density of about 1 every 2 nm^2 in graphene by oxygen plasma, the fracture strength drops 10 times compared to the pristine graphene. [9] This indicates that although one point defect in an entire sample would have only a small effect, when there is a significant number of such defects, the strength can be dramatically lower than the ideal value. Since there are many fold structures and the broken spots in the graphene sheet, they might be contributing to lowering the strength in a critical way.

On the other hand, the breakage occurs more likely to the **Scheme 2b** than **Scheme 2a** case. In **Scheme 2b**, the fold structure is randomly broken forming the bilayer regions and linear shaped crack which is highlighted by blue dashed circle. In the ongoing research by other member in Ruoff's group, Da Luo, according to the high-resolution transmission electron microscope (TEM) image, it has a high probability (eight of ten specimens) that the fold-structures are broken in a way of **Scheme 2b**. [Manuscript in preparation] Therefore, based on this model, we can regard the defect caused by the broken fold structure as a linear-shaped defect. Accordingly, we can also investigate the stress concentration factor of the crack in the fold structure based on this crack information.

Let's assume that the linear atomic-scale crack's length is 20 nm based on the research from Da Luo. [Manuscript in preparation] From the equation (2), the stress which graphene can endure is 0.131 σ_c based on QFM. Although we set the value of σ_c as 130 GPa, which is the highest reported strength of pristine graphene [1], the endurable stress of the graphene specimen is only 17 GPa, which is drastically decreased from its intrinsic strength. Therefore, we can think that the crack made by the broken graphene fold structure could be a critical flaw to lower the graphene's overall mechanical property.

Based on the assumption and theoretical calculation, we could estimate the effect of the defect in the graphene fold structure to the overall mechanical property. We expect that it can role as a critical flaw which can decrease the global strength of the graphene. To understand the effect of the defects experimentally, we attempted to locate the exact region of folds and to do the tensile testing in well-defined regions in micro scale. Although the nanoindentation method is guaranteed to measure the graphene's mechanical performance well, the uniaxial tensile loading should be done to control the direction of applying stress and study about the effect of the crack.

2. Experimental method & Materials

2.1 Materials

The MEMS Push-to-Pull (PtoP) stage was provided by professor Juyoung Kim's group (UNIST) based on the design of the PtoP stage of Hysitron. [10] The C4 polymethylmethacrylate (PMMA) was purchased from Microchem and the gold metal source was purchased from iTasco.

2.2 Transferring graphene with supporting material on the silicon wafer
2.2.1 Transferring graphene supported by PMMA on the silicon wafer

The monolayer single-crystal graphene was grown by chemical vapor deposition on the both sides of a home-made single crystalline copper foil. [2, 11] The graphene coated copper foil was cut into 1x1 cm pieces and PMMA was spin-coated on one side of the graphene/copper foil at 9000 rpm for 30 seconds. Next, the foil was floated on ammonium persulfate (0.3M) solution for 10 minutes so that the PMMA coated side is on the top surface. Next, the assembly was then picked up to remove the graphene on the non-PMMA coated side by scrubbing the surface. The foil was then floated on the etchant again to remove all of the copper, then the graphene-PMMA composite was washed of etchant residues by transferring and floating on a separate container of DI water (30 minutes), repeating twice. After that, the sample was transferred on the back side of silicon wafer so that we can easily detach the sample during the loading process to the PtoP device. The transferred sample was dried overnight.

2.2.2 Transferring graphene supported by gold on the silicon wafer

The graphene was grown as described in **section 2.2.1** then it was cut into squares 1x1 cm. Approximately 300-nm thickness of gold was deposited on one side of graphene by thermal evaporation (ULTECH). After that, the assembly was floated on ammonium persulfate (0.3M) solution for 10 minutes so that the gold deposited side is on the top surface. Next, it was then picked up to remove the graphene on the non-gold coated side by scrubbing the surface. The foil was then floated on the etchant again to remove all of the copper, then the graphene-gold composite was washed of etchant residues by transferring and floating on a separate container of DI water (30 minutes), repeating twice. After the cleaning process, the sample was flipped in the DI water so the sequence of composite was changed from 'Gold-top & Graphene-bottom' to 'Graphene-top & Gold-bottom' so that the graphene fold structure could be observed in the SEM. The flipped composite was transferred on the back side of silicon wafer for easy detachment during loading of specimen on the PtoP stage. The transferred composite was dried overnight in ambient condition.

2.3 Loading the graphene-gold composite on the MEMS Push-to-Pull device

This section will focus on graphene-gold composite's loading process because we cannot see the graphene fold-structure in the graphene-PMMA composite specimen due to the sequence which was 'PMMA-top & graphene bottom'.
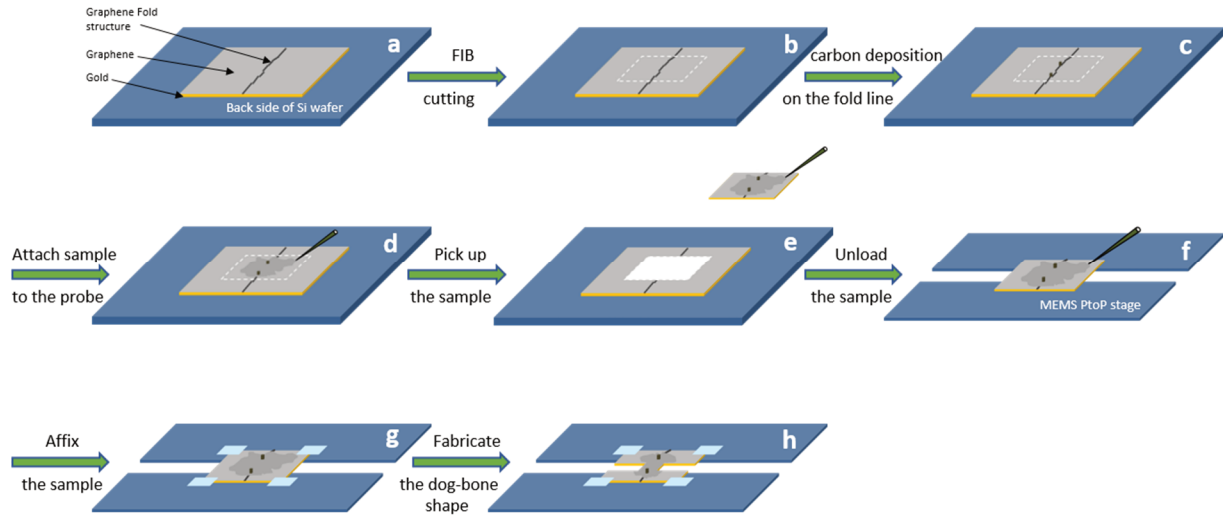
Scheme 3. Loading of graphene-gold composite on the PtoP device and fabrication of dog bone specimen using FIB.

The loading process was mainly done in a FEI SEM (Helios 450) which has focused ion beam (FIB) function and micro probe system. The overall scheme of this loading process is depicted in **Scheme 3**. (a) First, the graphene fold-structure was found in the SEM, and (b) was cut into a 10 μm * 10 μm size based on the fold-structure's location using FIB cutting. (c) Next, we deposited the carbon dot to mark the exact location on the both end of the graphene fold-structure. As later carbon deposition will be used to attach the specimen to the probe, carbon will inevitably cover the fold structure. (d) The sample was attached to the micro probe by carbon deposition. (e) Then, the sample was picked up from the silicon substrate and (f) unloaded on the PtoP stage's gap spot for the tensile loading. (g) The sample was affixed on the stage by depositing Pt on each vertex of specimen. (h) Next, a dog-bone shape was cut on the specimen and the sample was ready for tensile testing. The two types of dog-bone pattern configuration are described in **Figure 2**.
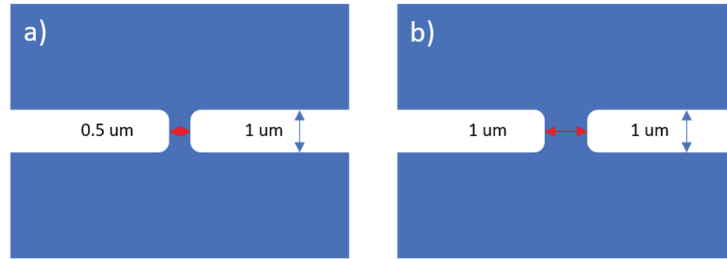
Figure 2. Two types of dog-bone pattern's configuration. (a) 0.5 um and (b) 1 um of gauge width.

Pattern (a) was used to fabricate the dog-bone specimen of graphene-PMMA composite and type (b) was used for the graphene-gold composite. In the case of the graphene-PMMA composite, the same method was used as described for the graphene-gold composite, but as the fold structure on these samples can't be observed, a random location was chosen to define the testing region.

2.4 In-situ SEM micro-tensile testing of the graphene-gold composite

The fabricated graphene-gold specimen underwent in-situ tensile loading by using the picoindentor (PI-87 from Hysitron) and observed by SEM (FEI Quanta 200 FEG). [12] The stage was held on a special holder of the SEM instrument and pushed by the picoindentor at a rate of 4 nm/s and 2 nm/s in the case of graphene-gold composite and graphene-PMMA composite, respectively.

2.5 Characterization

The deposited gold layer's thickness was measured by Bruker atomic force microscope (Dimension Icon with ScanAsyst). The stress-strain curve from the tensile loading test was obtained by Hysitron software and the strain calculation was done by digital image correlation (DIC). [12]

3. Result & Discussions

3.1 Stress-strain curve of graphene-PMMA composite

First, we measured the graphene-PMMA composite's mechanical property and tried to extract the pure graphene's one by using the 'rule of mixtures'. The stress-strain curve of graphene-PMMA composite and the corresponding SEM images used in DIC method is described in **Figure 3.**
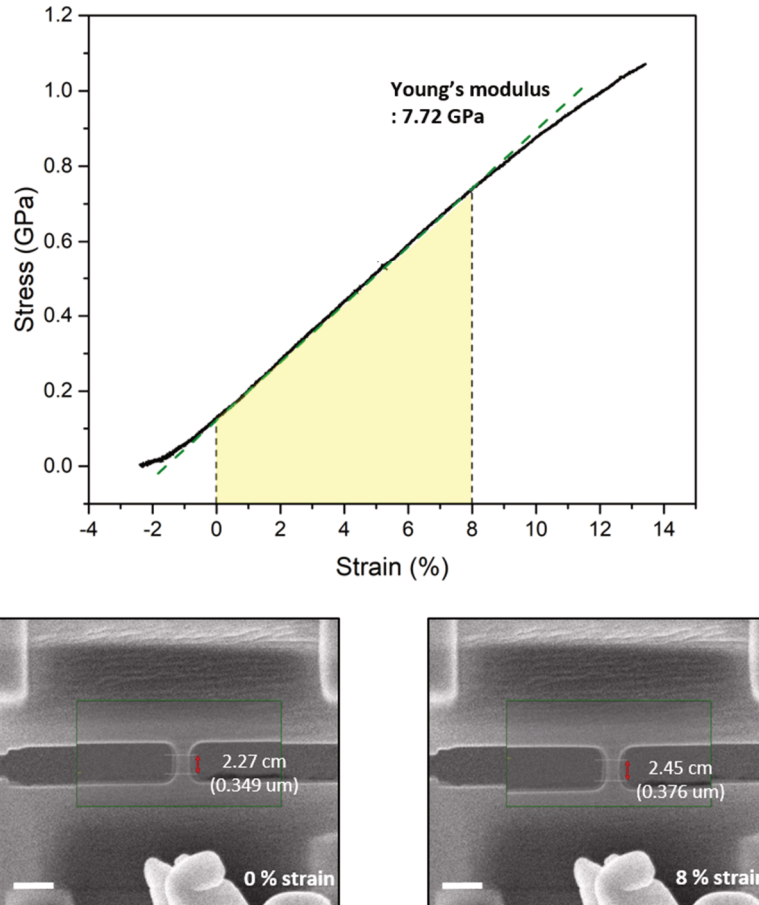
Figure 3. Graphene-PMMA composite's stress-strain curve and the corresponding SEM images used in DIC method.

According to the curve in Figure 3, the measured Young's modulus was 7.72 GPa, the fracture strength was 1.1 GPa and the specimen was elongated linearly until 8% of strain. For the rule of mixture, we had to measure the pure PMMA layer's mechanical property, but the pure PMMA dog-bone specimen was too weak to measure and experimental data could not be obtained. The literature value for the Young's modulus of PMMA is reported as 3.30 GPa. [13] If the thickness of single layer graphene is approximated to 0.34 nm, we can extract the Young's modulus of graphene using the rule of mixtures (Equation (3))

$$E_{G\text{-PMMA}} = E_G \frac{t(G)}{t(G)+t(PMMA)} + E_{PMMA} \frac{t(PMMA)}{t(G)+t(PMMA)} \tag{3}$$

where $E_{G\text{-PMMA}}$ and E_G are the Young's modulus values for the graphene-gold composite and gold, respectively and t(G) and t(PMMA) are the thickness of graphene and gold, respectively. According to the calculation, the extracted graphene's Young's modulus and tensile strength is 2.97 TPa which is much higher than the 1.0 TPa reported by James Hones' group. [1]

Those data are not effective at all because of following two reasons; First, we don't have any pure PMMA film's modulus and fracture strength value in our platform, so we cannot use rule of mixture with the obtained data. Because although the Young's modulus is an intrinsic property, due to the different geometry of the dog-bone specimen and proportion of defects according to the changed scale, the modulus value is changed. However, the maximum reported Young's modulus of PMMA is 5.0 GPa which is too small (accounting also for its thickness, and thus more aptly—for its contribution to the overall stiffness of the composite PMMA/graphene piece), so I attribute the abnormally high Young's modulus value to carbonaceous material deposited onto sample in the region being loaded (the "gauge length"). [14] Second, even though we can solve the first problem, there was no change in the slope of the curve at within 0.8% strain region. [15] If the graphene is fractured during the tensile testing, there must be a change of slope in the stress-strain curve mostly at around 0.8% strain region, but nothing was detected.

There is another weakness during operation of the FIB system to cut, load and unload the graphene-PMMA composite specimen. We observed a serious burning and rolling problem due to the electron beam's high energy. Usually, the PMMA layer is on the top side of the specimen, so the sample is very vulnerable to the electron beam which resulted inaccurate fabrication of dog-bone specimen. To avoid this problem, we also flipped the sequence of the composite such that the graphene was on the top surface. Although we could see the graphene fold structure, the PMMA layer underneath the graphene started to boil, which damaged the graphene. These issues are depicted in **Figure 4**. Accordingly, we searched for candidates which may provide a conductive supporting material which is both resistant to the high energy beam and has enough rigidity to prevent the rolling

issue and allow the modulus to be measured experimentally. In this aspect, gold fits these requirements because it is an electrically conductive metal, and has a proper Young's modulus (a reported value of 4.43 GPa obtained from testing a 300-nm thick Au film) to extract the graphene's information. [16]
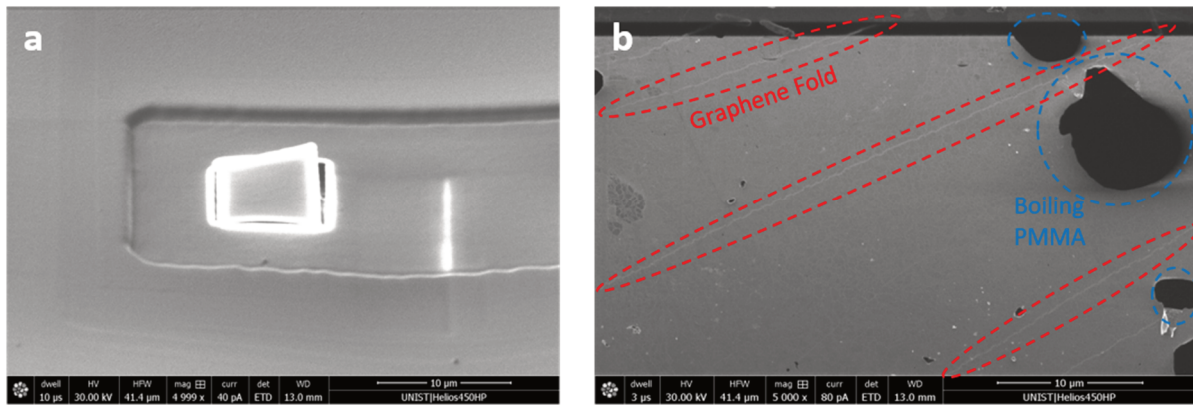
Figure 4. (a) Rolling problem of graphene-polymer composite under SEM environment and (b) bursting PMMA beneath the graphene in the flipped sequence.

3.2 Stress-Strain curve of gold film and graphene-gold composite

We obtained the stress-strain curve of four different specimens; the pure-gold specimen, the graphene-gold composite without any fold structure, the graphene-gold composite with a straight and intact fold structure, and the graphene-gold composite with a broken fold structure. In **Figure 5**, those stress-strain curves are described, and their Young's modulus is shown in the **Table 1**.
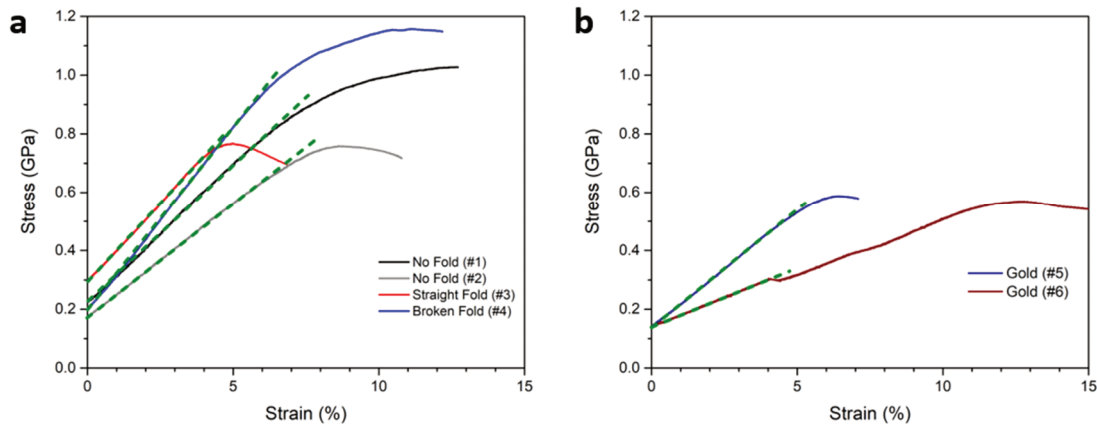
Figure 5. Stress-strain curve of (a) graphene-gold and (b) gold dog-bone specimen.

According to the curve we obtained, the specimen was linearly deformed until about 5 % and there is no change of slope around the 1% region. In previous report, graphene could be elongated only until 0.8 % of strain without fracture [15], but in the experiment, our specimens strain in the linearly elongated region was from 4 % to 6 % which is much higher than the graphene alone can withstand but still there was no change of the slope. Therefore, we don't know at which point the graphene is fractured, so the fracture strength and Young's modulus value of graphene could not be obtained. Based on this, we can conclude that the 285 nm thickness of gold is too strong to extract the graphene's information like the PMMA's case. Moreover, due to the incorrect data from limited number of specimens, it is difficult to figure out the graphene's exact information as well.

3.3 Intrinsic limitation from the instrument

3.3.1 Poor resolution of SEM

In the DIC process, the length of the gauge before and after the tensile loading is measured manually. In this analysis, SEM images are loaded on a Powerpoint slide and the gauge length measured "by eye". In this method, due to the low resolution of SEM, it is difficult to estimate the exact length of the gauge during tensile measurements and there is a high possibility to make an error calculating the strain value. **Figure 6** highlights the possible error of gauge lengths by the location of the defining lines.
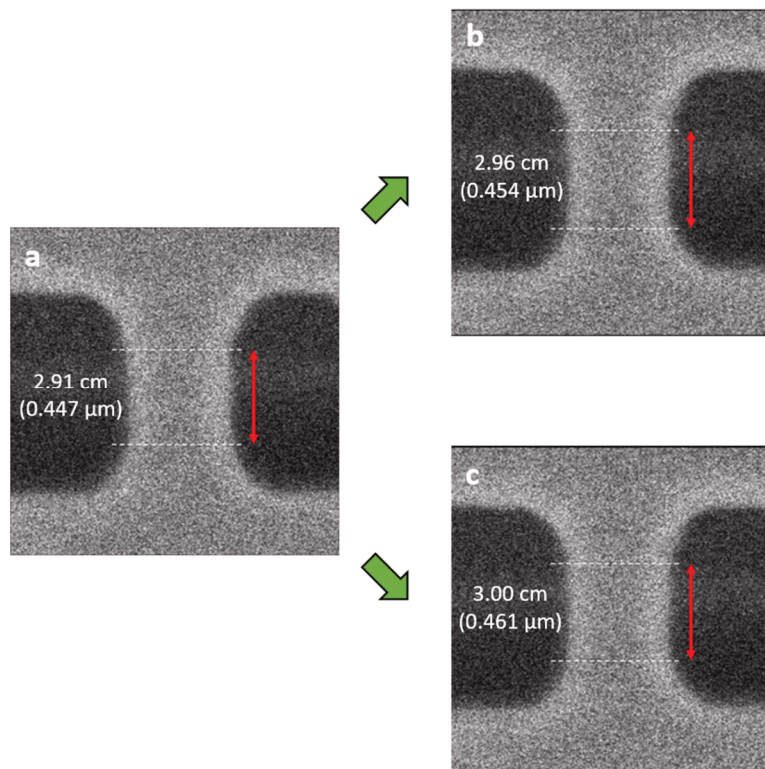
Figure 6. SEM images of the DIC process for sample #3 highlighting the sensitivity of measuring the gauge length "by eye". (a) The gauge length used for DIC before tensile testing. (b-c) Differently measured gauge lengths by choosing different locations in DIC process after the tensile testing.

According to those figures, although the **Figure 6b** and **6c** are the same elongated specimen's SEM images, because of the low resolution, the gauge length of the tensile loaded sample could be interpreted ambiguously, where the strain could be calculated into 1.72 % and 3.10%, respectively.

3.3.2 Broad deposition of platinum and carbon

During the loading of graphene-gold composite onto the PtoP device, carbon and platinum deposition was used. When the specimen was picked up, carbon deposition was used to stick the specimen to the microprobe and platinum was deposited on each vertex to affix the specimen onto the PtoP device. However, the principle of deposition using FIB is that the metal or carbon gas (in the case of our instrument (FEI Helios 450s), naphthalene gas) is blown on the sample thus the deposited region is much wider than the intended region. The effect of the deposition is illustrated in **Figure 7**.
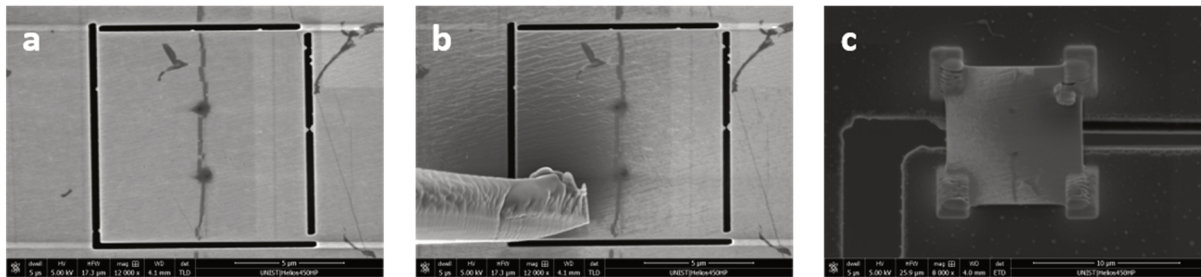
Figure 7. The effect of the broad deposition of carbon using FIB. (a) Original sample. (b) After attachment of specimen to the microprobe. (c) Covering the graphene fold region (gauge spot) by the deposition.

As shown in the figures, the carbon deposition covers the gauge length. This can cause the contamination on the gauge length and resulting in inaccurate measurement of mechanical properties due to specimen thickness changes. According to the literature, a particular type of 100-nm thick film carbon had a reported Young's modulus of 400 GPa [17] and platinum was reported to have a Young's modulus of 116 GPa [18], so only a 100-nm thick films of these materials would mean that the rule of mixtures method could not be used to obtain the mechanical properties of graphene. Moreover, the graphene fold structure cannot be found in the SEM for in-situ tensile loading as the resolution is insufficient. If the graphene fold structure could be seen in the higher resolution instrument, it would be possible to check the region of the graphene which underwent failure during strain.

3.4 Conclusion and suggestion for further research

In this chapter, polymer (PMMA) and metal (gold) were used as a supporting layer for tensile measurements. In the case of the polymer, degradation of the supporting film during exposure to the conditions inside the SEM, renders it unsuitable to be used as a supporting layer. In the case of gold, we failed to get the exact fracture strength and Young's modulus of graphene with the fold structure by several factors; errors due to the high mechanical performance of supporting material which overwhelms the graphene's one, insufficient imaging resolution, contamination by the deposition of carbon and platinum, the high thickness of gold compared to the graphene layer, and small number of samples giving inadequate statistics. To improve the result, it is necessary to change the thickness or the material of the supporting layer. It is rationalized that a thickness of several hundred nanometers of gold is not sufficient for supporting the graphene. 150 nm thickness of gold was also tried but it had the same rolling issue under SEM environment as was observed in the case of PMMA due to its thin thickness. Therefore, it is required to find the other thin film material which can endure the high energy of both the electron and ion beam and is also strong enough to support the graphene but not overwhelming the graphene's one. One reasonable candidate could be a sputtered carbon thin film, which exerts about 210 GPa of Young's modulus and 7 MPa of fracture strength at 10 to 20 nm thickness. [17] Based on the data, the sample could have high rigidity at extremely thin thickness and is safe in SEM environment. Therefore, it can bring an advantage in terms of sample fabrication.

The carbon deposition problem during the sample attachment to the microprobe must be solved—it completely defeats useful measurements, now. One solution is to increase the specimen size during the FIB cutting step and deposit the carbon far from the gauge region during the picking-specimen-up process. Then, if the resolution issue of SEM is solved during the in-situ tensile loading, we can directly observe the graphene-fold structure's changes during the testing, allowing the exact location of the failure point to be observed and either assigned to the fold region or another part of the graphene film.

Prof. Ruoff has thus suggested that we consider methods for mechanical testing that avoid all use of ion beams—either in preparing the sample or imaging it before or while testing. In-situ bulge testing of monolayer polycrystalline graphene was reported by *Yun, et al.*.[19] They transferred monolayer graphene onto a silicon wafer device containing a number of holes (10-90 μm in diameter) and thereby suspended the graphene over the hole(s). With a home-built instrument, they could apply a pressure difference to the graphene membrane forming a bulge. This method applies uniform stress to the graphene membrane. According to the method reported by *Yun, et al.*, one can also get the fracture strength of the graphene membrane that is tested.

To explore the microstructure of ultrathin film is highly challenging. However, if the single crystalline graphene's critical flaw which causes the difference of strength between the micro and

macro scale is demonstrated, it will help to step forward to understand the graphene's defect and finally, the defect-free graphene sheet can be produced exerting its intrinsic high mechanical performance even in the practical field.

4. References

1. Lee, C., et al., *Measurement of the elastic properties and intrinsic strength of monolayer graphene.* 2008. **321**(5887): p. 385-388.

2. Wang, B., et al., *Camphor-Enabled Transfer and Mechanical Testing of Centimeter-Scale Ultrathin Films.* 2018. **30**(28): p. 1800888.

3. Grantab, R., V.B. Shenoy, and R.S. Ruoff, *Anomalous strength characteristics of tilt grain boundaries in graphene.* Science, 2010. **330**(6006): p. 946-8.

4. Wang, M.C., et al., *Effect of defects on fracture strength of graphene sheets.* Computational Materials Science, 2012. **54**: p. 236-239.

5. Huang, M., et al., *Highly Oriented Monolayer Graphene Grown on a Cu/Ni(111) Alloy Foil.* ACS Nano, 2018. **12**(6): p. 6117-6127.

6. Inglis, C.E., *Stresses in a plate due to the presence of cracks and sharp corners.* Proc. Inst. Naval Arch., 1913. **55**.

7. Meyers, M.A.e. and K.K. Chawla, *Mechanical behavior of MATERIALS.* Second ed. 2009, New York: CAMBRIDGE UNIVERSITY PRESS.

8. Pugno †, N.M. and R.S. Ruoff ‡, *Quantized fracture mechanics.* Philosophical Magazine, 2004. **84**(27): p. 2829-2845.

9. Zandiatashbar, A., et al., *Effect of defects on the intrinsic strength and stiffness of graphene.* Nat Commun, 2014. **5**: p. 3186.

10. Oh, Y., et al., *MICRO/NANO-MECHANICAL TEST SYSTEM EMPLOYING TENSILE TEST HOLDER WITH PUSH-TO-PULL TRANSFORMER* U.S. Patent, Editor. 2014, Hysitron Incorporated, Eden Prairie, MN (US).

11. Jin, S., et al., *Colossal grain growth yields single-crystal metal foils by contact-free annealing.* Science, 2018. **362**(6418): p. 1021-1025.

12. Park, S.-Y., et al., *Nanolaminate of metallic glass and graphene with enhanced elastic modulus, strength, and ductility in tension.* Scripta Materialia, 2017. **139**: p. 63-66.

13. Ishiyama, C. and Y. Higo, *Effects of humidity on Young's modulus in poly(methyl methacrylate).* Journal of Polymer Science Part B: Polymer Physics, 2002. **40**(5): p. 460-465.

14. *Material Properties of Polystyrene and Poly(methyl methacrylate) (PMMA) Microspheres.* 2015 [cited 2019 18 June]; Available from: https://www.bangslabs.com/sites/default/files/imce/docs/TSD%200021%20Material%20Properties%20Web.pdf.

15. Ni, Z.H., et al., *Uniaxial strain on graphene: Raman spectroscopy study and band-gap opening.* ACS Nano, 2008. **2**(11): p. 2301-5.

16. Neugebauer, C.A., *Tensile Properties of Thin, Evaporated Gold Films.* Journal of Applied Physics, 1960. **31**(6): p. 1096-1101.

17.   Tsukamoto, Y., H. Yamaguchi, and M. Yanagisawa, *Mechanical properties of thin films: Measurements of ultramicroindentation hardness, Young's modulus and internal stress.* Thin Solid Films, 1987. **154**(1-2): p. 171-181.

18.   Abbas, K., et al., *Nanoscale size effects on the mechanical properties of platinum thin films and cross-sectional grain morphology.* Journal of Micromechanics and Microengineering, 2016. **26**(1).

19.   Hwangbo, Y., et al., *Fracture characteristics of monolayer CVD-graphene.* Sci Rep, 2014. **4**: p. 4439.

Acknowledgement

First of all, I would like to express my sincere appreciation to my advisor, Professor Rodney S. Ruoff. Thanks to his support and guidance, I could learn how to think when I am working in the research field. Especially, I was inspired by his energetic movement to figure out what he wants to know and lots of knowledge he owns. For me to become an expert in the field, his behavior will be a model of mine always. It was my honor to have done my Master's degree under his guidance. I would also thank to the other committee members of my Master's degree defense, Professor Hyeonsuk Shin and Professor Hajin Kim for being my examiners and giving various comments, taking their time from their busy schedule. Especially, for Prof. Kim, I appreciate his sincere comments in my experiment and advice for my future. It was my pleasure to work with his group.

My genuine gratitude also goes to Dr. Kipom Kim, who is a senior researcher in the Korean Brain Research Institute. He is such a talented engineer in not only his main field, but also the other fields which he is interested in. It was a great experience to work with him and I am really glad to have met him in my graduate school life. I sincerely hope and I am quite confident that he will do marvelous work and be a great inventor in his future. I also thank Ms. Gayoung Lee for giving a lot of support during my business trips and advice for my graduate life. I hope she has a happy and delightful life as she always is. I also want to appreciate Mr. Sihyoung Loh in Prof. Kim's group for helping me to use their magnetic tweezer system. I hope he can spend his graduate life well and achieve great scientific progress.

I also want to express my heartfelt appreciation to Dr. Bin Wang. From Dr. Bin, I learned how to overcome any difficulties cleverly. Whenever he faced a problem, he always looked back to his method and immediately tried to find a breakthrough by changing his original idea. This basis inspired me in the whole of my work as well as my life. I will always keep in mind this and it was my luck to work and meet Dr. Bin in my life.

My sincere appreciation also goes to my lab members. Dr. Da Luo, Dr. Sunghwan Jin and Dr. Benjamin Cunning always give a lot of helpful and sincere advice whenever I ask many questions, guide me to study my field thoroughly and think scientifically. Meihui Wang and Yunqing Li always kindly helped me breakthrough when I was having a hard time during research. Finally, Jaehong Seo and Hyunju Nam, thanks to their emotional support, I could spend my graduate life so happily and hopefully. Without these members, I couldn't reach this level of scientific achievement. I really thank them so much and truly hope their future will be bright.

I really appreciate my family for their continuous support and love. I lastly want to appreciate my friends, Hongbeom Lee and Sungho Kim for spending whole time with me in UNIST. I could refresh and be happy with them during my time in UNIST. Thank you.